Supplementary Material for
"Deterministic entanglement of photons in two superconducting microwave resonators"

H. Wang,[1, 2] Matteo Mariantoni,[1] Radoslaw C. Bialczak,[1] M. Lenander,[1] Erik Lucero,[1] M. Neeley,[1] A. D. O'Connell,[1]
D. Sank,[1] M. Weides,[1] J. Wenner,[1] T. Yamamoto,[1, 3] Y. Yin,[1] J. Zhao,[1] John M. Martinis,[1] and A. N. Cleland[1, *]

[1]*Department of Physics, University of California, Santa Barbara, CA 93106, USA*
[2]*Department of Physics and Zhejiang California International NanoSystems Institute,*
Zhejiang University, Hangzhou 310027, China
[3]*Green Innovation Research Laboratories, NEC Corporation, Tsukuba, Ibaraki 305-8501, Japan*

MATERIALS AND METHODS

The device fabrication is similar to that published previously [1]. The half-wavelength superconducting coplanar waveguide resonators are made of rhenium deposited on a c-axis single-crystal sapphire substrate, with a 5 μm-wide center signal trace and 10 μm gaps to the ground plane metallization on either side of the center trace. We place a single lithographed shorting strap connecting the two ground planes at the midpoint of each resonator to improve the quality of the grounding. This point is a voltage node for the fundamental half-wave resonant mode, so that there is minimal additional dielectric loss from the shorting strap's underlying amorphous Si insulating film [2].

In the circuit layout (image in Fig. S1), the coupling resonator C is designed to have a higher resonance frequency than the two state storage resonators A and B. This prevents the qubit frequencies from having to cross the C resonator frequency during NOON state amplification. The two storage resonators A and B are designed with slightly different resonance frequencies, to avoid possible interference between the resonators. The full frequency span in the design was chosen to be close to 550 MHz, within the dynamic range of our custom microwave electronics.

The two superconducting phase qubits and coplanar waveguide resonators are fabricated together, using our standard multi-layer process [3]. The phase qubit consists of a 2 μm^2 Al/AlO$_x$/Al junction in parallel with a 1 pF Al/a-Si:H/Al shunt capacitor and a 720 pH inductance loop (design values) [4]. The critical current of the Al/AlO$_x$/Al junction is approximately 2 μA. We use interdigitated coupling capacitors between the qubits and the resonators, designed to each have a capacitance of 1.9 fF. The actual coupling strengths vary slightly with resonator frequency; the detailed component parameters are listed in Table S1.

Devices were cooled down in a dilution refrigerator with a base temperature of about 20 mK, giving negligible thermal excitation in relation to the qubit and resonator operation frequencies; thus the qubits and resonators relax to their quantum ground states. Signal
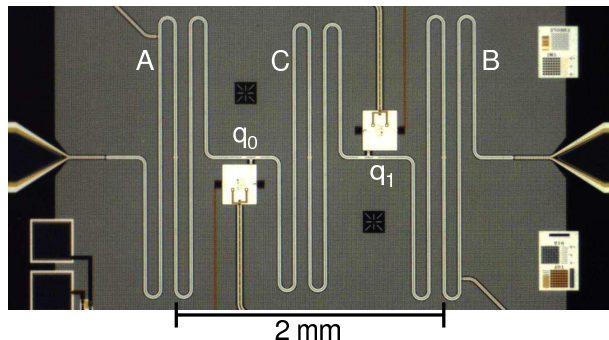

FIG. S1: (Color online) Optical micrograph shows three half-wavelength coplanar resonators A, B and C (sinusoidal traces) and two qubits q_0 and q_1. The coupling resonator C is between the two qubits, and the photon-state storage resonators A and B are on either end of the circuit. The resonators are 8 to 9 mm long, yielding 6 to 7 GHz resonance frequencies (see Table S1 for exact values). The center-to-center distance between the storage resonators is ~ 2 mm.

lines are heavily filtered with either microwave attenuators (for microwave and high frequency pulse lines) or resistor-capacitor low-pass filters and copper-powder microwave filters (for low-frequency signal lines) [3]. A custom microwave arbitrary waveform generator was used to generate pulses with sub-nanosecond resolution for the pulse envelopes [5], which are essential for optimal qubit control.

GENERATION SEQUENCE TUNE-UP

The time required for each qubit-resonator i-SWAP is calibrated separately. The swap times obtained from these calibrations scale correctly as $\sqrt{n}$ with the number of photons n in the resonator [5] and also depend on the state of the qubit. Examples of the swap calibrations for a one-photon swap between qubit q_0 and resonator A are shown in Fig. S2, for both the $|g\rangle \leftrightarrow |e\rangle$ and $|e\rangle \leftrightarrow |f\rangle$ transitions. The swap time for the $|e\rangle \leftrightarrow |f\rangle$ transition is approximately $1/\sqrt{2}$ times that for the $|g\rangle \leftrightarrow |e\rangle$ transition. This scaling is as expected, as the multi-level phase qubit can be well-approximated as a weakly nonlinear

circuit component	f_r (GHz)	$f_{|g\rangle\leftrightarrow|e\rangle}$ (GHz)	$f_{\text{nonlinear}}$ (GHz)	T_1 (ns)	T_ϕ (ns)
A	6.340	-	-	3500	$\gg T_1$
B	6.286	-	-	3300	$\gg T_1$
C	6.816	-	-	3400	$\gg T_1$
q_0	-	~ 6.65	≈ 0.20	450	$200-300$
q_1	-	~ 6.58 or 6.68	≈ 0.20	320	$200-300$

Coupling strength	$q_0 \leftrightarrow A$	$q_0 \leftrightarrow C$	$q_1 \leftrightarrow B$	$q_1 \leftrightarrow C$
g/π (MHz)	17.8	20.0	17.4	20.0

TABLE S1: Resonator and qubit parameters. The qubit parameters are quoted for when the qubits are off-resonance (see below). The qubit nonlinearity $f_{\text{nonlinear}}$ is the frequency difference between the $|g\rangle \leftrightarrow |e\rangle$ and $|e\rangle \leftrightarrow |f\rangle$ transitions. The phase coherence time T_ϕ is obtained using a Ramsey interference experiment, which yields the Ramsey time T_2, from which we calculate $1/T_\phi = 1/T_2 - 1/(2T_1)$. T_ϕ measured for resonators similar to those used here [6] satisfies $T_\phi \gg T_1$; we assume the same applies here. T_ϕ for the qubits decreases with increasing length of the pulse sequence due to the $1/f$ nature of the phase noise. For most state generation sequences used in this experiment, of typical length 50 to 100 ns, the qubit T_ϕ is in the range of 200 to 300 ns. Coupling strengths correspond to the measured splitting in frequency units, with g appearing in the Hamiltonian shown in Eq. (S1).

harmonic oscillator for the energy levels confined by the qubit's metastable potential well. The scaling confirms that we can use harmonic-oscillator-like raising and lowering operators for the three-level qubit, as was done in the numerical simulations (see below).

Figure S3 shows the detailed pulse sequence used to generate and measure the $N = 2$ NOON state. Sequence steps in general are calibrated and checked separately to maximize preparation fidelity, when possible. For example, we first optimize the qubit Bell state preparation at the end of step I in the preparation sequence detailed in Fig. S3. The fidelity for the Bell state is above 0.80, with entanglement of formation 0.59, which agrees well with numerical simulations, performed using a pure dephasing time $T_\phi = 300$ ns for the qubits (see below). State tomography of the qubits is also as expected: Fig. S3(b) shows the density matrices extracted from coupled qubit tomography, measured at different times during the $N = 2$ NOON state preparation. We note that at the end of the sequence, both qubits should return to their ground states. Experimentally we observe small populations in the excited states $|e\rangle$ due to decoherence and pulse imperfections. The exact qubit state after the NOON state generation is measured and is used as the initial state for the qubits when performing Wigner tomography on the storage resonators (see below).

NUMERICAL SIMULATIONS

Numerical simulations were performed using the model Hamiltonian

$$
\begin{aligned}
H =\ & \sum_{q_i=q_0,q_1} H_{q_i} + \sum_{j=A,B,C} \hbar\omega_j \left(b_j^+ b_j + \frac{1}{2} \right) \\
& + \sum_{(q_i,j)} \hbar g_{q_i\leftrightarrow j} \left(a_{q_i}^+ b_j + a_{q_i} b_j^+ \right) \\
& + \sum_{q_i=q_0,q_1} \frac{1}{2}\hbar \left[\Omega_{q_i}(t) a_{q_i}^+ + \Omega_{q_i}(t)^* a_{q_i} \right], \quad \text{(S1)}
\end{aligned}
$$

where H_{q_i} is the Hamiltonian of the qubit q_i, $a_{q_i}^+$ and a_{q_i} (b_j^+ and b_j) are the raising and lowering operators for the 3-level qubit q_i (resonator j), $g_{q_i\leftrightarrow j}$ is the coupling strength between qubit q_i and resonator j, with a sum over all possible qubit-resonator combinations, such that $(q_i,j) \in \{(q_0,A),(q_0,C),(q_1,B),(q_1,C)\}$ and $\Omega_{q_i}(t)$ is the time-dependent, two-tone ($f_{|g\rangle\leftrightarrow|e\rangle}$ and $f_{|e\rangle\leftrightarrow|f\rangle}$) microwave drive on qubit q_i.

The 3-level qubit Hamiltonian H_{q_i} was approximated as

$$
H_{q_i} = \begin{bmatrix} 0 & 0 & 0 \\ 0 & hf_{|g\rangle\leftrightarrow|e\rangle} & 0 \\ 0 & 0 & hf_{|g\rangle\leftrightarrow|f\rangle} \end{bmatrix}_{q_i}, \quad \text{(S2)}
$$

where for simplicity we assumed a constant nonlinearity $f_{|g\rangle\leftrightarrow|e\rangle} - f_{|e\rangle\leftrightarrow|f\rangle} = 200$ MHz, so that $f_{|g\rangle\leftrightarrow|f\rangle} \simeq 2f_{|g\rangle\leftrightarrow|e\rangle} - 200$ MHz. We approximated the multi-level qubit $a_{q_i}^+$ and a_{q_i} by the raising and lower operators for the lowest three levels of a harmonic oscillator, as discussed above.

Decoherence was approximated using the Lindblad master equation taking into account the Markovian environment [7], where two characteristic decay times, the
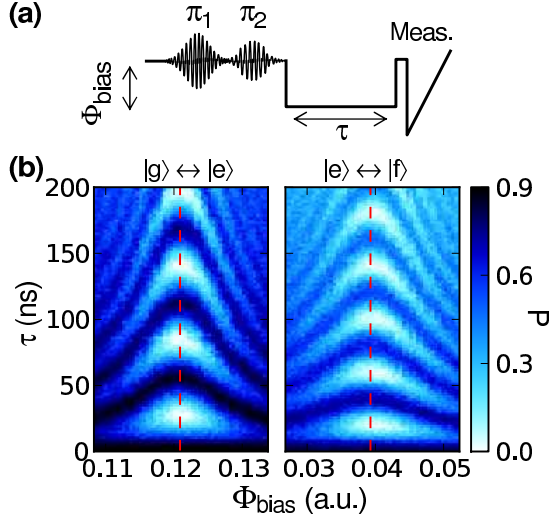
(a)

(b)

FIG. S2: (Color online) One-photon swaps between qubit q_0 and resonator A. (a) Pulse sequence for measuring swaps between the qubit $|e\rangle \leftrightarrow |f\rangle$ transition and resonator A. When off-resonance, the qubit is excited by a pair of π pulses, with the first pulse π_1 taking the qubit from $|g\rangle$ to $|e\rangle$ and the second pulse π_2 making the transition from $|e\rangle$ to $|f\rangle$. The qubit $|e\rangle \leftrightarrow |f\rangle$ transition is then tuned close to resonance with resonator A and the qubit and resonator left to interact for a time τ. The triangular pulse at the end is used to measure the probability of the qubit being in the $|f\rangle$ state at the end of the sequence. (b) Left: Qubit $|g\rangle \leftrightarrow |e\rangle$ swaps with resonator A. The qubit is prepared as in (a), but without the second pulse π_2. The qubit $|e\rangle$ probability (color bar) is plotted as a function of interaction time τ and frequency tuning Φ_{bias}. Oscillations in probability are due to the qubit excitation swapping with the resonator. Right: Qubit $|e\rangle \leftrightarrow |f\rangle$ swaps with resonator A; the preparation of the qubit is as in (a) and the plot shows the $|f\rangle$-state probability as a function of interaction time τ and qubit flux bias Φ_{bias}. Red dashed lines indicate the on-resonance Φ_{bias} values used in the experiment. The swap frequency for the on-resonance $|e\rangle \leftrightarrow |f\rangle$ transition is $1.403 \approx \sqrt{2}$ times that for the on-resonance $|g\rangle \leftrightarrow |e\rangle$ transition.

energy relaxation time T_1 and the pure dephasing time T_ϕ, were used for each resonator and qubit.

The simulations do not directly account for the non-Markovian $1/f$ character of the phase noise in the qubits. To account for this, we used a sequence-time dependent T_ϕ for each qubit, as obtained from Ramsey interference measurements. We used $T_\phi = 300$ ns for ∼50 ns-long sequences and $T_\phi = 200$ ns for ∼100 ns-long sequences. The resulting simulations agree reasonably well with the experimental measurements.

BIPARTITE WIGNER TOMOGRAPHY

Displacement Pulses

The bipartite Wigner tomography is an extension of a method described elsewhere [5, 6, 8]. We displace each resonator with Gaussian pulses $|\alpha\rangle$ and $|\beta\rangle$ (resonator A and B, respectively), with variable phase and amplitude. The values of α and β are distributed over several concentric circles in the complex plane, centered on the origin, where the distribution of values varies approximately with the size N of the NOON state. The radii of the circles run through the set $r_j \in \{0, 0.2, 0.7, 0.9, 1.3\}$, in square-root of photon number units [5]. The pulse values are evenly distributed on each circle, with complex values $r_j \exp(i2\pi\ell/N_{r_j})$, where ℓ ranges from 1 to N_{r_j} and N_{r_j} is an integer ranging from 1 ($r_j = 0$), 5 or 6 ($r_j = 0.2$), up to 9 to 15 ($r_j = 1.3$), depending on the number of photons in the NOON state.

We use every possible combination of values of α and β distributed over the circles of the same radius for tomography, i.e., for each value of α, we use all β values with the same amplitude as α. The total number of displacement pulse combinations is thus quite large and increases with the photon number N in the NOON state, typically involving of order a few hundred pulses. The displacement pulses can be expressed as

$$
\begin{aligned}
D_{AB}(\alpha_j, \beta_k) &= D_A(\alpha_j) \otimes D_B(\beta_k) \\
&= e^{\alpha_j b_A^+ - \alpha_j^* b_A} \otimes e^{\beta_k b_B^+ - \beta_k^* b_B} .
\end{aligned} \tag{S3}
$$

Photon Populations

For an initial joint-resonator density matrix ρ_{initial}, the displacement pulses shift the density matrix to

$$
\rho = D_{AB}(-\alpha_j, -\beta_k)\rho_{\text{initial}}D_{AB}(\alpha_j, \beta_k) . \tag{S4}
$$

By bringing both qubits (initially in their $|g\rangle$ states) on resonance with the resonators, the joint number states contained in two resonators, i.e., the diagonal elements of ρ, can be read out, as each diagonal element swaps with the qubits at a different rate [5], resulting in a distinct time-dependence for the probabilities P_{gg}, P_{ge}, P_{eg}, and P_{ee}. These can be numerically simulated using the device parameters from Table S1.

As displayed in Fig. S3(b), there is a small non-zero occupation of the excited state of each qubit after the state generation sequence, due to decoherence and pulse imperfections. We use the measured qubit state after the state generation sequence as the qubit initial condition when numerically simulating the tomography. Using these simulations, we obtain the time dependence for the each of the probabilities P_{gg}, P_{ge}, P_{eg}, and P_{ee} corresponding to different combinations
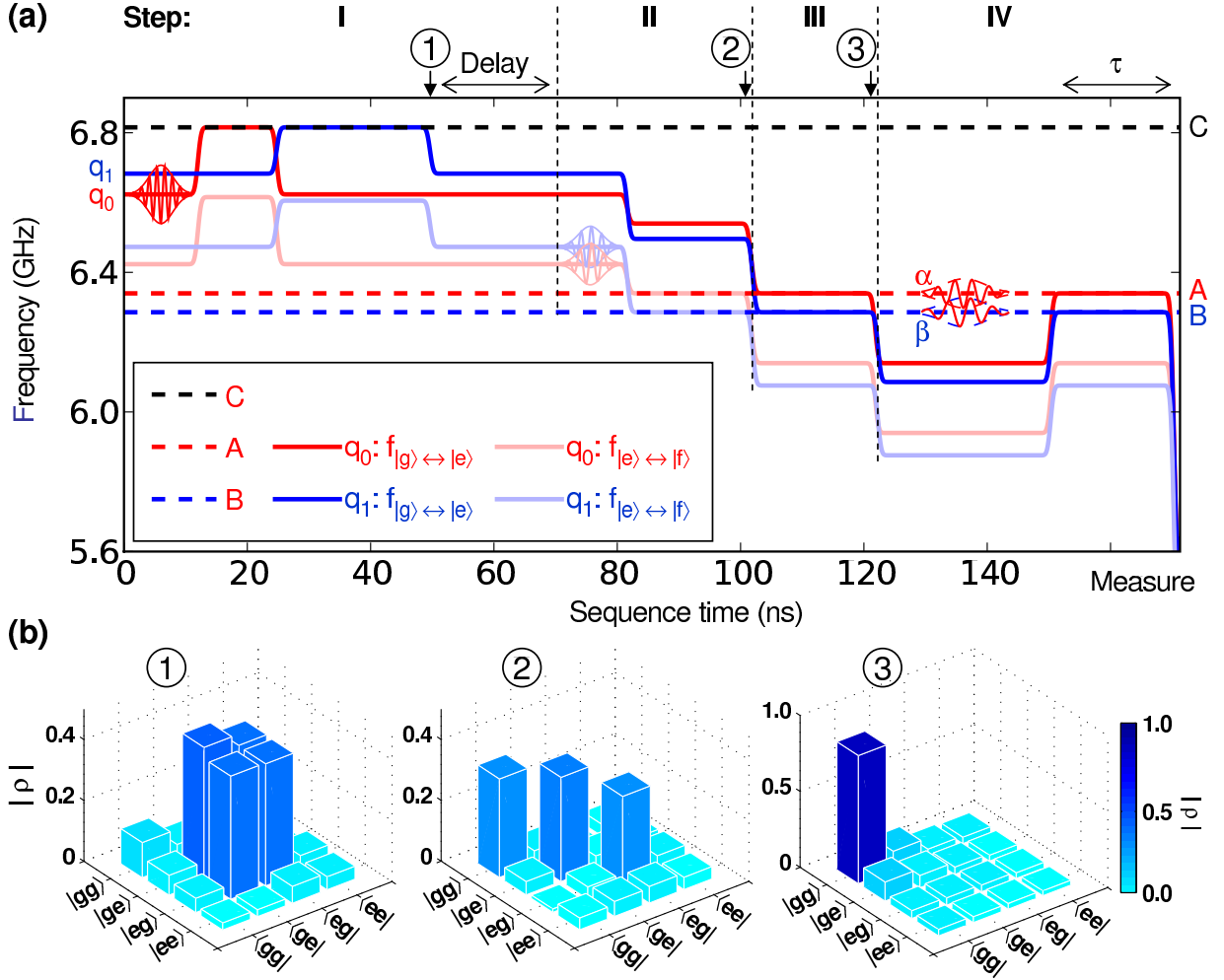
FIG. S3: (Color online) NOON state preparation. (a) Sequence to generate and measure $N = 2$ NOON state. Qubit transition frequencies $|g\rangle \leftrightarrow |e\rangle$ (dark-color solid lines) and $|e\rangle \leftrightarrow |f\rangle$ (light solid lines) are tuned to control coupling of each qubit to resonators (dashed lines); q_0 in red, q_1 in blue. Vertical lines divide sequence into steps; circled numbers indicate points where qubit tomography was performed. Step **I**: A $\pi_{|g\rangle \to |e\rangle}$ pulse excites q_0 to $|e\rangle$, followed by a $\sqrt{i\text{-SWAP}}$ entangling q_0 and resonator C. A full i-SWAP between C and q_1 disentangles the resonator and generates the qubit Bell state $|eg\rangle + |ge\rangle$. For the $N = 1$ NOON state this entanglement is transferred to the storage resonators (not shown). For $N > 1$, $\pi_{|e\rangle \to |f\rangle}$ pulses excite each qubit to yield $|fg\rangle + |gf\rangle$. Both qubits' $|e\rangle \leftrightarrow |f\rangle$ transitions are then tuned to the respective storage resonators, and an i-SWAP transfers one photon to the resonators. For $N = 3$, this is repeated to transfer a second photon (not shown). In step **III**, both qubits' $|g\rangle \leftrightarrow |e\rangle$ transitions are tuned to the resonators and an i-SWAP transfers the remaining excitation to the resonators, completing the generation, leaving both qubits in their ground states. Step **IV**: State analysis. The storage resonator A (B) is displaced in phase space by a Gaussian pulse $|\alpha\rangle$ ($|\beta\rangle$), followed by an on-resonance interaction with each qubit's $|g\rangle \leftrightarrow |e\rangle$ transition for a time τ, followed by joint-qubit state readout. Many repetitions of this sequence are combined to generate joint-qubit state probabilities P_{gg}, P_{ge}, P_{eg}, and P_{ee} versus τ. The joint-qubit state probabilities can be used to obtain the two-resonator density matrix (see text). (b) Qubit density matrices extracted from tomography at circled points in (a). (1) Qubit Bell state. (2) Qubit state after transferring first photon into resonators. This is a state with qubits and resonators entangled, so the density matrix is as expected. (3) Qubit state after $N = 2$ NOON state generation. Both qubits are very nearly in their ground states, and thus can be used to measure the resonators.

of photon number (Fock) states in the two storage resonators. Examples of these probability traces are shown in Fig. S4(a) for some selected initial states. The time-dependent traces for these probabilities, for the set of Fock states $\{|m\rangle_A |n\rangle_B, m = 0, 1, 2, \ldots, n = 0, 1, 2, \ldots\}$, are then used to decompose the experimentally-measured time traces, which yields the probability distribution for the Fock number states contained in the storage resonators. This thus yields the diagonal elements of the experimentally-measured displaced density matrix ρ.

We obtain the diagonal elements of ρ by doing a least-squares fit of the time-dependent probabilities, corrected for measurement fidelity. We use the MATLAB packages YALMIP and SeDuMi for the fitting. The num-

ber of fitting parameters is the number of diagonal elements, directly determined by the maximum photon number state contained in the resonators, plus the number of photon quanta added by the displacement pulses $|\alpha\rangle$ and $|\beta\rangle$. Fits are done with constraints $P_{mn} \geq 0$ and $\sum_{m,n} P_{mn} = 1$ to return meaningful probability values. Examples of these fits are shown in Fig. S4, for the $N = 1$ NOON state.

Joint-Resonator Density Matrices

With the diagonal elements of ρ measured for a set of displacements $\{D_{AB}(\alpha_j, \beta_k)\}$, ρ_{initial} can be solved for by inverting Eq. (S4) through a linear least-squares fit, while restricting the density matrix to be Hermitian. The resulting density matrices may have small negative eigenvalues due to noise. We use the MATLAB packages YALMIP and SeDuMi to perform semi-definite convex optimization programming, allowing us to find a physical density matrix that is closest to the actual matrix.

When solving for ρ_{initial} of a NOON state, we restrict the dimension of ρ_{initial} to an $N \times N$ matrix, even though the dimension of ρ can be significantly larger than this due to the displacement pulses. We zero-pad the elements in ρ_{initial} that have photon indices larger than N. This approach is validated by the coincidence measurements (see main text), as we do not detect any frequency components for number states above N prior to injecting a displacement pulse.

NOON STATE DECAY DYNAMICS

The Wigner tomography allows us to study the decoherence dynamics of the bipartite system [6]. The experimental results, compared with numerical simulations, are shown in Fig. S5, with relevant elements in Table S2. We note that the time evolution of the off-diagonal elements in the two-resonator density matrix, which represent inter-resonator coherence, is different from the evolution of the corresponding off-diagonal elements for a single resonator, which represent intra-resonator coherence [6].

Error Analysis

Statistical errors in the qubit probability measurements as well as uncertainty in the amplitude calibration for the displacement pulses α_j and β_k are used to estimate the uncertainty in the amplitude and phase of each density matrix element. These errors are found to be small, in part because the constraints on the analysis filters unrealistic values. Instead we find that slow phase drifts in the electronics, perhaps dominated by ambient

Delay (ns)	$\langle 01|\rho|01\rangle$	$\langle 10|\rho|10\rangle$	$\langle 01|\rho|10\rangle$	$\Delta|\langle 01|\rho|10\rangle|$
16	0.36(1)	0.386(9)	0.328-0.037i	0.009
250	0.31(1)	0.32(1)	0.31+0.01i	0.01
500	0.32(1)	0.31(1)	0.285-0.068i	0.009
750	0.27(1)	0.27(1)	0.259+0.017i	0.008
1000	0.27(1)	0.28(1)	0.261+0.010i	0.008
1250	0.23(1)	0.24(1)	0.215-0.037i	0.008
1500	0.24(1)	0.23(1)	0.229-0.033i	0.008
2000	0.20(1)	0.20(1)	0.198+0.001i	0.006
2500	0.17(1)	0.17(2)	0.155-0.005i	0.008
3000	0.14(2)	0.15(2)	0.13+0.04i	0.01
4000	0.08(2)	0.09(4)	0.06+0.03i	0.01

TABLE S2: Density matrix elements as a function of delay time for the $N = 1$ NOON state shown in Fig. S5. Uncertainties for the diagonal elements are in parentheses, while the magnitude of the uncertainty for the off-diagonal terms are given in the last column.

temperature fluctuations, give the main phase uncertainties, especially during long measurements. Evaluating a single density matrix usually takes a relatively short time during which these drifts are minimal. However, measuring a series of density matrices such as Fig. 5 in the main paper, takes a much longer time, typically 12 to 20 hours, allowing for more significant drifts. These mostly affect the phases of the density matrix elements, rather than the amplitudes.

Validation

The bipartite Wigner tomography was validated by several consistency checks. (1) The density matrix is as expected for a range of different states, including the highly entangled NOON states, the energy eigenstates $|2\rangle_A|0\rangle_B$ (Fig. S6(a)), the separable (product) state $(|0\rangle - |1\rangle)_A(|0\rangle - |1\rangle)_B$ (Fig. S6(b)) and the unentangled mixed states (see below). (2) The NOON states display the expected phase sensitivity as a function of photon number N, as shown in Fig. 5 in the main paper and Table S3. (3) The NOON state fidelity and entanglement of formation agree reasonably well with numerical simulations. (4) The time-dependence of the density matrix elements, showing uniform exponential decay of all elements, is as expected and agrees with numerical simulations, as shown in Fig. S5 and Table S2. (5) The calculated negativities are significantly above zero for the NOON states and precisely zero (within the measurement error) for the unentangled mixed state (see below).

We note that bipartite Wigner tomography can measure any matrix element with a relatively high accuracy, as we can displace the system by an arbitrary amount in phase space. Even for relatively small off-diagonal ele-
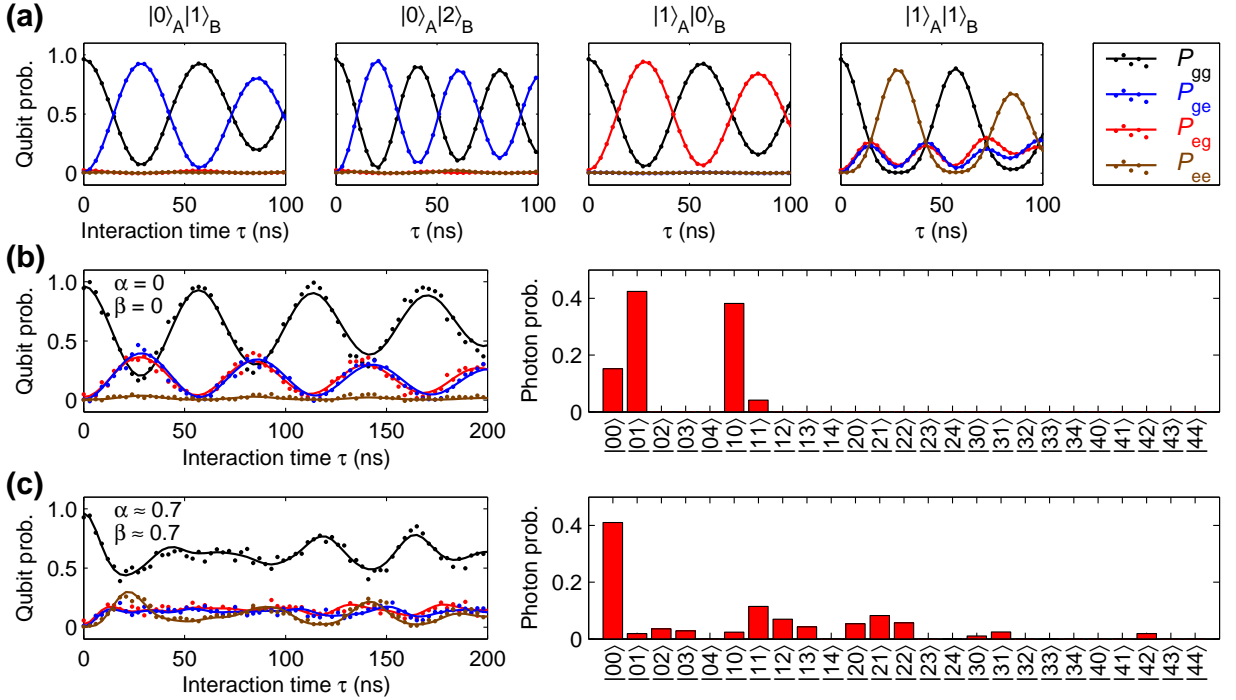
FIG. S4: (Color online) Joint-state probabilities and photon number distribution analysis for $N = 1$ NOON state. (a) Joint-qubit state probabilities from numerical simulations, for a few selected initial resonator states in A and B, as indicated. Lines are a guide to the eye. Device parameters are as in Table S1. (b) Left panel, measured joint-qubit state probabilities for null displacement pulses $\alpha, \beta = 0$. Lines are fits to the data. The fit joint-photon probability distributions $\rho_{|m\rangle_A|n\rangle_B}$ are displayed in the right panel. The most significant occupations are in $|0\rangle_A|1\rangle_B$ and $|1\rangle_A|0\rangle_B$, as expected for this state. (c) Left panel, measured joint-qubit state probabilities for the displaced state with $\alpha = 0.7$ and $\beta = 0.7$ (square-root of photon number units). Lines are fits to the data. The fit joint-photon probability distributions $\rho_{|m\rangle_A|n\rangle_B}$, shown in the right panel, are significantly different from those shown in (b) due to the displacement. The matrix elements for the higher photon number states are omitted for viewing, although these may not be negligible for larger displacement pulses.

	color	$\langle 01|\rho|01\rangle$	$\langle 10|\rho|10\rangle$	$\langle 01|\rho|10\rangle$
	black	0.327	0.460	-0.229+0.239i
Fig. 5(a)	blue	0.318	0.464	0.204+0.200i
	red	0.301	0.439	0.196-0.156i

TABLE S3: (Color online) Density matrix elements for the data shown in Figs. 5(a) of the main paper, coded by color (uncertainties not shown). The phase uncertainty in the off-diagonal elements is dominated by the slow phase drift of our electronics (see text).

ments, such as the desired off-diagonal term in the $N = 3$ NOON state, the tomography can unambiguously evaluate this element and measure its sensitivity to external phase perturbations.

Ensemble of Mixed States

We use a synthetic ensemble of mixed states to illustrate the hazards involved in relying purely on coincidence measurements for demonstrating NOON-state en-tanglement. The ensemble comprises a mixture of 50% $|1\rangle_A|0\rangle_B$ and 50% $|0\rangle_A|1\rangle_B$ states, i.e., an ensemble with the same probability of being measured in either of the states forming the $N = 1$ NOON state, but without any entanglement. This is done by generating the pure state $|1\rangle_A|0\rangle_B$ and measuring the time-dependent joint probabilities $P_{gg}(\tau)$, $P_{ge}(\tau)$, $P_{eg}(\tau)$, and $P_{ee}(\tau)$ for this state. We then generate the other component of the ensemble, the pure state $|0\rangle_A|1\rangle_B$, and repeat the generation and measurement procedure. Each value of τ involves 300 repeats of the preparation and measurement sequence for each of the pure states. We then combine the measurement results with equal weights, creating the joint probabilities for the synthetic ensemble; these data are shown in the main paper. The tomographic analysis yielding the density matrices is done in the usual way. The outcome of the ensemble measurements are shown in the main text, with the joint probabilities evolving in a way indistinguishable from the entangled NOON states, but the density matrix for the ensemble revealing a complete lack of entanglement, as witnessed by the negligible values for the off-diagonal elements.
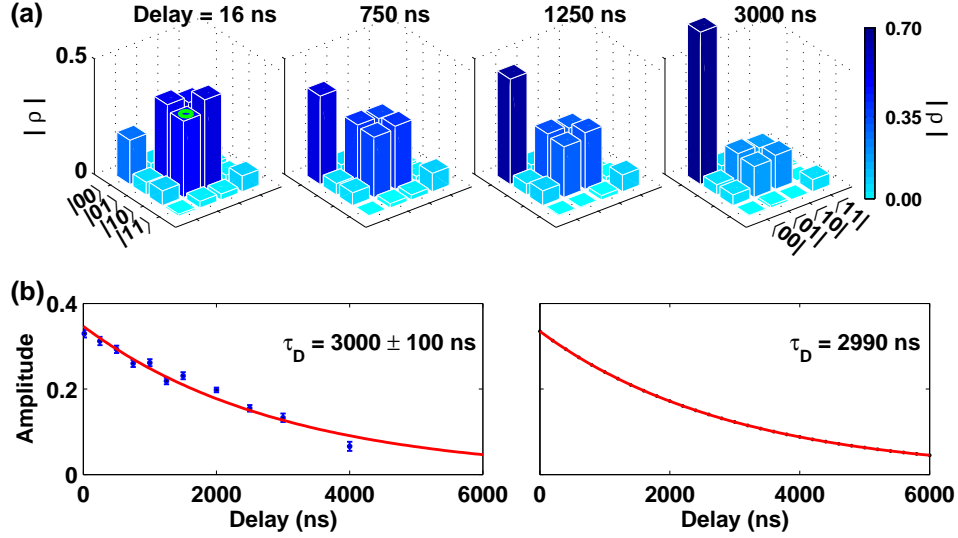
FIG. S5: (Color online) Decay of the $N = 1$ NOON state. (a) Density matrix amplitudes for the $N = 1$ NOON state at selected delay times. Bar heights and colors represent the matrix element amplitude, scale on right. The off-diagonal element amplitudes decrease at a rate close to that of the diagonal counterparts. Values for the relevant elements are tabulated in Table S2. (b) Left: Experimental data, showing amplitude of the off-diagonal element as marked by a green ellipse in the first panel in (a), plotted versus post-preparation time. Line is a fit yielding a single decay time τ_D, consistent with a Markovian dissipative environment [9]. Right: Numerical simulation of the same density matrix element as the experiment, with the line an exponential fit. The simulation uses the measured density matrix as the initial condition and the resonator T_1 value listed in Table S1. The simulated decay time τ_D is in good agreement with experiment.
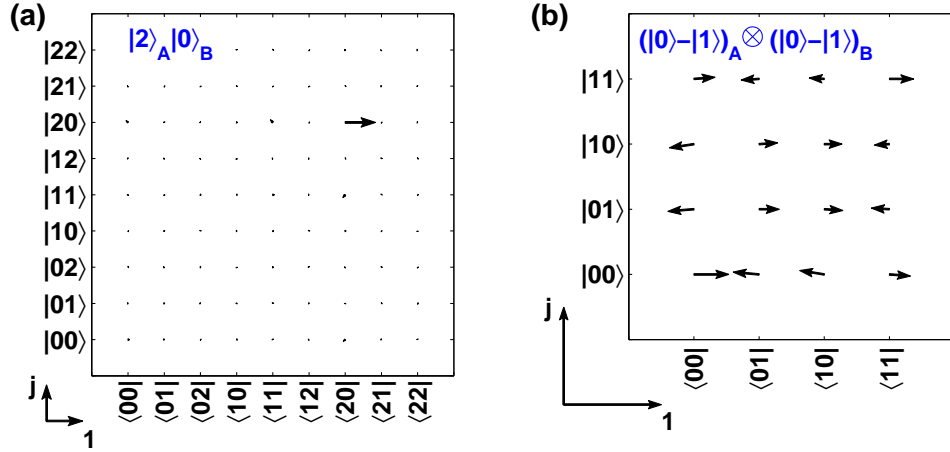

FIG. S6: (Color online) Benchmark resonator states used to validate the bipartite Wigner tomography. (a) Photon-number representation of the two-resonator density matrix (error bars not shown), for the energy eigenstate $|2\rangle_A|0\rangle_B$, generated by pumping two photons into resonator A while leaving B in its ground state. The magnitude of each matrix element is represented by the full length of the corresponding arrow and the phase angle determined by the direction of the arrow in the complex plane (scale on bottom left). Density matrix is as expected from state preparation. (b) Two-resonator density matrix (error bars not shown) for the test resonator state $(|0\rangle - |1\rangle)_A(|0\rangle - |1\rangle)_B$, generated by creating the $|g\rangle - i|e\rangle$ state in each qubit, followed by a complete i-SWAP transfer to each storage resonator. Non-idealities are likely due to inaccuracies in the preparation pulses.

MOON STATE

The NOON-state generation protocol can be simply generalized to generate MOON states, with different photon numbers in the two entangled resonators. The generation is similar to the NOON state sequence shown in Fig. S3. We assume $M > N$: After generating the Bell entanglement between two qubits at the end of step I (Fig. S3(a)), we repeat step II $N − 1$ times, yielding the four-fold entangled state $|eg(N−1)0\rangle + |ge0(N−1)\rangle$. The photon amplification and transfer process (step II) is then applied $M − N$ times, but only to qubit q_0 and resonator A, yielding the state $|eg(M − 1)0\rangle + |ge0(N − 1)\rangle$. The final qubit excitations are then transferred in step III,
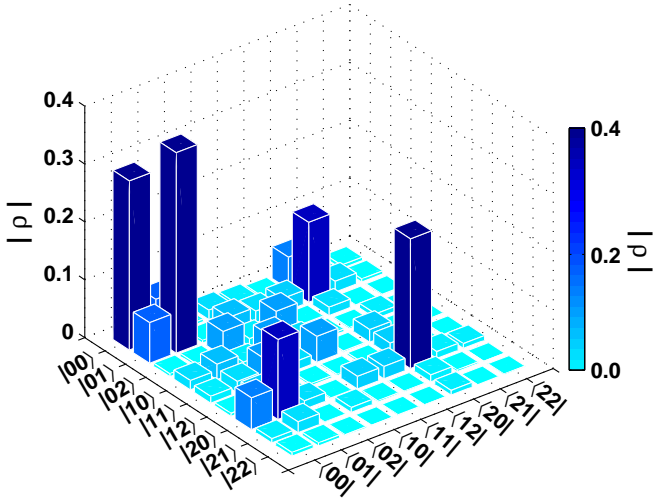
FIG. S7: (Color online) Measured density matrix (errors not shown) of the MOON state with $M = 2$ and $N = 1$. The generation sequence is as described in the text. The state fidelity is 0.42 ± 0.01, lower than our typical NOON state fidelity, due to technical issues with the particular device used for this experiment; the entanglement of formation is 0.16. The negativity is $N_e = 0.14 \pm 0.01$, indicating a statistically significant entanglement.

resulting in the MOON state $|gg\rangle \otimes (|M0\rangle + |0N\rangle)$, with the qubits disentangled from the resonators. A MOON state generated in this fashion, with $M = 2$ and $N = 1$, is shown in Fig. S7.

* To whom correspondence should be addressed. E-mail: anc@physics.ucsb.edu
[1] H. Wang *et al.*, *Phys. Rev. Lett.* **101**, 240401 (2008).
[2] A. D. O'Connell *et al.*, *Appl. Phys. Lett.* **92**, 112903 (2008).
[3] J. M. Martinis, *Quantum Information Processing* **8**, 81 (2009).
[4] M. Neeley *et al.*, *Phys. Rev. B* **77**, 180508R (2008).
[5] M. Hofheinz *et al.*, *Nature* **459**, 546 (2009).
[6] H. Wang *et al.*, *Phys. Rev. Lett.* **103**, 200404 (2009).
[7] G. Lindblad, *Commun. Math. Phys.* **48**, 119 (1976).
[8] D. Leibfried *et al.*, *Phys. Rev. Lett.* **77**, 4281 (1996).
[9] D. F. Walls and G. J. Milburn, *Phys. Rev. A* **31**, 2403 (1985).